Submit to J. of Electrochemical Society

Evaluation of the electrochemo-mechanically induced stress in all-solid-state Li-ion batteries

Hong-Kang Tian[1], Aritra Chakraborty[1], A. Alec Talin[2], Philip Eisenlohr[1], Yue Qi[1, *]

[1]Department of Chemical Engineering and Materials Science, Michigan State University, East Lansing, 48824, USA

[2]Sandia National Laboratories, Livermore, CA 94551, USA;

Abstract

The mechanical degradation of all-solid-state Li-ion batteries (ASSLBs) is expected to be more severe than that in traditional Li-ion batteries with liquid electrolytes due to the additional mechanical constraints imposed by the solid electrolyte on the deformation of electrodes. Cracks and fractures could occur both inside the solid electrolyte (SE) and at the SE/electrode interfaces. A coupled electrochemical-mechanical model was developed and solved by the Finite Element Method (FEM) to evaluate the stress development in ASSLBs. Two sources of volume change were considered, namely the expansion/shrinkage of electrodes due to lithium concentration change and the interphase formation at the SE/electrode interface due to the decomposition of SEs. The most plausible solid electrolyte decomposition reactions and their associated volume change were predicted by density functional theory (DFT) calculations. It was found that the stress associated with a volume change due to solid electrolyte decomposition can be much more significant than that of electrode volumetric changes associated with Li insertion/extraction. This model can be used to design 3D ASSLB architectures to minimize their internal stress generation.

---

* Tel: 517-432-1243; Email: yueqi@egr.msu.edu

1 Introduction

Most Li-ion battery electrode materials experience volume changes during lithiation and de-lithiation. The Li compositional inhomogeneity causes stress, which is referred to as the "diffusion-induced stress" and leads to mechanical failure of electrodes during battery cycling. As the mechanical fractures and the structural disintegration result in battery capacity loss, models to predict the mechanical degradation of the electrodes were established and developed, either at the single-particle level or the electrode composite level, especially in the past decade for traditional Li-ion batteries [1-13]. With the increasing interest in all-solid-state Li-ion batteries (ASSLBs) [14-18] owing to their improved endurance and safety, their mechanical degradation becomes a critical and unsolved issue that impacts the performance and life of ASSLBs [19].

The mechanical degradation of ASSLBs is expected to be more severe than that of traditional Li-ion batteries, since the solid electrolyte (SE), unlike the mechanically compliant liquid electrolyte, imposes additional mechanical constraints on the deformation of electrodes. Indeed, cracks have been observed in the solid electrolytes and at the electrode/electrolyte interfaces in ASSLBs. For example, cracks and fractures were found across the $Li_{1+x}Al_xGe_{2-x}(PO_4)_3$ (LAGP) solid electrolyte caused by the growth of the interphase during electrochemical cycling of symmetric Li/LAGP/Li coin cells [20]. The LAGP/Li metal interface in a symmetric Li/LAGP/Li coin cell was also found to undergo amorphization and volume expansion, which causes fracture of the SE along with a massive increase in impedance [21, 22]. Interface delamination of a $LiNi_{1-x-y}Co_xMn_yO_2$ (NMC) electrode from a β-Li_3PS_4 SE in a composite positive electrode was observed during charging, as the interfacial decomposition of the sulfide SE and the contraction of NMC [23] caused a loss of interfacial contact and resulted in capacity loss [24, 25]. Despite its importance, a modeling framework to evaluate the coupled electrochemical-mechanical stress generation has not been fully established for ASSLBs.

The mechanical constraints highly depend on ASSLB architecture [26]. It is expected that the stress distribution will be different in 2D thin-film batteries that have planar geometries [27], in 2.5D batteries with one planar and one needle-like structure [28], and 3D batteries with fully interdigitated electrodes and SEs [29-31].

Various sources of chemical strain and the mechanical constraints imposed by the solid-state architecture contribute to the stress generation in ASSLBs. Solid electrolytes, especially those based on stiff ceramics, form imperfect contacts at the interfaces with the electrodes in ASSLBs, causing non-uniform local stress [24]. Chemical strain due to Li concentration-induced volume changes on one or both sides of the electrode/SE interface will directly lead to stress generation. Several numerical studies have tackled this source of chemical strain and its impact on the crack propagation in electrode–SE composite, electrode/SE interface delamination [32, 33], and damages to the electrodes [5]. The stress generation in ASSLBs is further complicated by the interphase layer that forms due to chemical reactions involving the electrode and solid electrolyte. Earlier reports claimed improved electrochemical stability for SEs compared to liquid electrolytes based on cyclic voltammetry (CV) measurements [34-36]. However, it was later revealed that many promising SEs decompose via reduction/oxidation reactions [37, 38] that form an interphase layer at the electrode/SE interface. Such interphase formation is accompanied by a volume change at the SE/electrode interface. As we shall show in this paper, this source of chemical strain can lead to relatively high stress generation.

The primary goal of this paper is to develop a general continuum modeling framework to evaluate the stress generation caused by (i) the volume changes in electrodes due to electrochemical reactions and (ii) the interphase layer due to the decomposition of solid electrolytes in ASSLBs as schematically illustrated in Fig. 1 for the chosen example of an ASSLB with nanoscale architecture (Fig. 1a). This specific 2.5D battery geometry [28] was fabricated by sputtering a $LiCoO_2$ positive electrode on substrates of conical micro-columns, followed by sputter-coating a Lithium Phosphorous Oxynitride (LiPON) electrolyte, and depositing a thin film Si negative electrode. Such an "egg carton" geometry is anticipated to reduce the Li diffusion length within the cathode and anode electrodes while increasing areal energy density, as has been demonstrated by experiments and continuum modeling [28]. The *in operando* stress development has not been investigated yet but is expected to be highly inhomogeneous across the 2.5D conical geometry and modulated by the presence (or absence) of voids in between the micro-columns.

In this paper, the continuum model will take inputs from both experiments and first-principles calculations. The volume change due to the decomposition of the SE will be obtained by assuming the products of the most energetically favorable reaction at Li chemical potential [37, 38]. These reaction energetics and volume changes can be calculated based on density functional theory (DFT) calculations. The constraints experienced within the 2.5D nanostructured ASSLB will be approximated by two limiting boundary conditions. This DFT-informed continuum model can be easily adapted for evaluating various electrode/SE materials 3D ASSLB geometries.

2 Computation methods

Simulations of charge transport and chemically induced stress in the selected battery geometry were carried out at the continuum level using the commercially available COMSOL Multiphysics software version 5.4 with two added-on modules of Electrochemistry and MEMS for the electrochemical and mechanical simulation, respectively. The input for the simulations can be found in the supporting materials. The distribution of the first principal stress in the ASSLB was used as a metric to determine the location of possible crack propagation and failures based on the maximum stress that can be generated. For the Finite Element Method (FEM), mesh refinement was conducted to check the convergence of the maximum first principal stress, as shown in Fig S-1 in the supporting material. A wide range of mesh parameters was tested (maximum element size, minimum element size, maximum growth rate, curvature factor, and the resolution of narrow regions), and the corresponding number of mesh elements ranges from 11,000 to 290,000. When the total number of mesh elements is over 200,000, the output stress converged within a 0.5% variation.

2.1 Battery Architecture

The hexagonally patterned (egg carton) battery architecture depicted in Figure 1a is approximated and represented by an axially symmetric geometry comprising the Si negative electrode, $LiCoO_2$ (LCO) positive electrode, and LiPON solid electrolyte as shown in Figure 1b. A scanning electron microscopy (SEM) characterization [36] revealed voids in between neighboring positive electrode humps but did not specifically measure their sizes. Therefore, two boundary conditions were adopted to study and bound the effect of the voids, namely a free-side and fixed-side boundary condition along the short horizontal and long vertical face on the left side of Figure 1b. All other outer boundaries are interfaces between electrodes and the current collector and the continuous electrolyte/electrode film. Those boundaries are restricted with respect to normal displacements (as indicated in Figure 1b). The internal boundaries of the interphase layers in the LiPON electrolytes have matching nodes at the interface to simulate a well-bonded interface formed by a Chemical Vapor Deposition (CVD) process.

2.2 Volume change induced by Li concentration gradient during charging

The diffusion-induced stress is caused by the Li compositional inhomogeneity during battery cycling. Therefore, the first part of the model is to calculate the Li concentration gradient during the battery charging process based on Newman's model [39, 40], which captures Li-atom diffusion in both electrodes, Li-ion migration and diffusion in the solid electrolyte, and the charge transfer reactions at the electrode/electrolyte interfaces. The interphase layers were not explicitly modeled as their impact on interface impedance is considered insignificant due to their nanometer-scale thickness.

In the positive LCO electrode and the negative Si electrode, the diffusion of Li atoms was described by Fick's law of diffusion [41]:

$$\frac{\partial C_{Li}}{\partial t} + \nabla(-D_{Li}\nabla C_{Li}) = 0 \qquad \text{Eq. 1,}$$

where C_{Li} is the local concentration of Li in electrodes and D_{Li} is the diffusion coefficient of Li in the Si electrode (D_{Li_Si}) and in the $LiCoO_2$ electrode ($D_{Li\_LCO}^{normal}$ and $D_{Li\_LCO}^{lateral}$), and these values are listed in Table A-1. The diffusion of Li is isotropic in Li_xSi and anisotropic in Li_yCoO_2, as reported previously [28]. According to a simulation that best fits the observed behavior [36], Li diffuses laterally along the LCO surface about three orders of magnitude faster than normal to it. The Li diffusion coefficient is assumed to be a constant through the simulation, assuming the deformations are too small to perturb the mass-transport.

In the LiPON SE, since both concentration and electrostatic potential gradients exist, the transport of Li ions was described by the Nernst–Planck equation [42]:

$$\frac{\partial C_i}{\partial t} + \nabla\left(-D_i \nabla C_i - Z_i \frac{D_i}{RT} F C_i \nabla \varphi_{electrolyte}\right) = 0 \qquad \text{Eq. 2,}$$

where C_i is the concentration of species i (either Li-ions or negative charges [24, 43]), D_i is the diffusion coefficient of species i, $\varphi_{electrolyte}$ is the solution potential, Z_i is the charge of species i, R is the gas constant, T is the absolute temperature, and F is the Faraday constant. To maintain charge neutrality in the solid electrolyte, the following condition was enforced everywhere in the electrolyte:

$$\sum Z_i C_i = 0 \qquad \text{Eq. 3.}$$

Note that there are no free electrons in the solid electrolyte. According to previous studies [43, 44], only the Li-ions are the mobile ions (transfer number = 1) in LiPON. It has been shown that the LiPON framework can accommodate uncompensated negative charges, but these charges are localized and nonmobile.

The charge transfer reactions at SE/electrode interfaces were described by Butler–Volmer kinetics [44], as the current density $i_{electrode}$ (unit: A/m^2) is driven by the overpotential η at the SE/electrode interface.

$$i_{electrode} = i^0_{electrode}\left[e^{-\alpha_{electrode}\frac{F}{RT}\eta} - e^{(1-\alpha_{electrode})\frac{F}{RT}\eta}\right] \qquad \text{Eq. 4,}$$

where α is the charge transfer coefficient and $i^0_{electrode}$ is the exchange current density at the electrochemical equilibrium. $i^0_{electrode}$ is further defined [45] as:

$$i_{electrode}^{0} = Fk_{electrode}\left[\frac{\left(C_{Li\_max} - C_{Li}\ \right)C_{Li^{+}}}{(C_{Li\_max} - C_{Li\_min})C_{Li^{+}}^{0}}\right]^{\alpha} \times \left[\frac{C_{Li}}{C_{Li\_max}}\right]^{1-\alpha} \qquad \text{Eq. 5,}$$

where $k_{electrode}$ is a kinetic constant, C_{Li_max} and C_{Li_min} are the maximum and minimum Li concentration in the electrode, $C_{Li^{+}}$ is the Li ion concentration in the SE, and $C_{Li^{+}}^{0}$is the initial concentration of mobile Li ions in the SE. η is the overpotential at the SE/electrode interface and described as:

$$\eta = \varphi_{electrode} - \varphi_{electrolyte} - E_{electrode} \qquad \text{Eq. 6,}$$

where φ is the electric potential and $E_{electrode}$ is the equilibrium potential of the electrode. Thus, the battery voltage is calculated from $\varphi_{positive\_electrode} - \varphi_{negative\_electrode}$.The equilibrium potentials $\mathrm{E}_{\mathrm{electrode}}$ at the negative and positive electrodes were inputs obtained from previously fitted numerical functions [45]. The impact of the mechanical stress on the $\mathrm{E}_{\mathrm{electrode}}$ is considered to be negligible in the current model. $\varphi_{\mathrm{electrolyte}}$ at the negative electrode was set to zero. All variables with subscript "electrode" have different values for the positive (LCO) and negative (Si) electrode, as listed in Table A-1 in the Appendix.

A galvanostatic (constant current) charge/discharge process requires that the total current I_{total} (unit: A) passing through the negative electrode/electrolyte interface and the positive electrode/electrolyte interface (as labeled in Figure 1) are equal:

$$I_{total} = \int_{\mathrm{Area}_{(\mathrm{negative\_electrode/electrolyte})}} \mathrm{i}_{\mathrm{negative}} = \int_{\mathrm{Area}_{(\mathrm{positive\_electrode/electrolyte})}} \mathrm{i}_{\mathrm{positive}} \qquad \text{Eq 7.}$$

Note that this boundary condition does not preclude the reaction rate and Li concentration to be non-uniform over the electrode surfaces. Boundary conditions of zero flux were adopted on all other surfaces. Through the charging process, a constant current density, $i_{electrode}$ (A/m^2), is applied. For 3D and 2.5D ASSLB, the area refers to the projected area, thus the cross-section area of the Si electrode on top of the $LiCoO_2$/LiPON (listed in Table A-1) was used to obtain the $i_{electrode}$.

This simulation first solved the time-dependent Li concentration profile in the ASSLB during the charging process. The voltage vs. capacity curves at different charging rates were calibrated with experiments to ensure reasonable Li concertation profiles were obtained. The charging process is terminated when the voltage reaches a specified cutoff voltage (4.2 volt in the charging process) or the Li concentration at any point in the electrodes reaches a concentration limit of either x = 3.75 in Li_xSi or y = 0.5 in Li_yCoO_2. These constraints imply no phase change nor diffusion coefficient change during the charge cycling simulation.

Snapshots of Li concentration profiles served as inputs for time-independent (static equilibrium) stress simulations to obtain the mechanical stress caused by the local Li concentration variation ΔC_{Li} in the electrodes. This assumption comes from the references [46, 47], in which the process of lithium diffusion in solids was found to be much slower than elastic deformation, so the mechanical equilibrium is established much faster than the diffusion process. Therefore, mechanical equilibrium can be modeled as a static equilibrium.

To simplify the model, the non-linear relation between relative volume change and Li concentration [4] is approximated by a proportionality

$$\Delta V_{Li} = a_v \Delta C_{Li} \qquad \text{Eq. 8}$$

The volume change in Li_yCoO_2 is relatively small and can be non-monotonic. The DFT predicted volume change Li_yCoO_2 exhibited different trends due to different DFT methods used. [3, 48-50] Here we adopted volume increases 2% when Li_yCoO_2 is fully lithiated [3], a trend that agrees with the more advanced DFT method with meta-GGA.[50] According to the previous study [3], Si expands by 263% when its composition changes from Si to $Li_{3.75}Si$. $LiCoO_2$ shows a 2% volume increase when its Li ratio changes from 0.5 to 1, so the volume expansion coefficient a_v can be determined. Although some research has considered the volume change in the solid-electrolyte due to Li concentration change, in this study, any volume change of the LiPON electrolyte is neglected, given its small overall change in Li concentration. Considering the maximum amount of mobile Li-ions is around 20% of the total Li in LiPON SE [43] and, as will be shown later, the Li-ion concentration changes by only less than 5% of the total Li in LiPON SE during the charging process.

2.3 Volume change induced by the decomposition of the solid electrolyte

The volume change due to the formation of two interphase layers was calculated based on the decomposition products that were the stable phases at the Li chemical potential at different state of charge. During the charging process, the Si electrode becomes more lithiated, and the equilibrium potential of Li (with respect to metallic Li) in Li_xSi (x = 0 to 4) decreases from 0.6 to 0.1. Similarly, the equilibrium potential of Li in Li_yCoO_2 (y = 1 to 0.5) increases (in the range of 2.5 to 4.2 V) with decreasing y in Li_yCoO_2. In this study, we selected Li_2PO_2N to represent LiPON, since it has been reported that the thin-film LiPON synthesized through Atomic Layer Deposition (ALD) is characterized as Li_2PO_2N [51, 52]. The equilibrium phases were obtained from the grand potential phase diagram introduced in [37, 38]. The corresponding decomposition reactions were obtained from the DFT-computed database in Material Project [53] queried through its Application Programming Interface (API) [54]. Different reaction routes and products of Li_2PO_2N correspond to different Li chemical potentials, as shown in Table 1. The unit volume of each solid compound was obtained from the Material Project database. The relative volume change for the decomposition reaction is defined as

$$\Delta V_d = \frac{V_2 - V_1}{V_1} \quad \text{Eq. 9,}$$

where V_1 and V_2 are the total volume of all reactants and products in the decomposition reaction, respectively.

The interphase can form during deposition or during cycling. To simulate the impact of growing interphase layers, two interphase layer thicknesses of 10 nm and 50 nm were chosen for this model, based on the typical thickness of Solid Electrolyte Interphase (SEI) in the range of 10–100 nm [55, 56], and an experimental study that suggested the thickness of LiPON/Si and Li/$LiCoO_2$ interfaces are both around 50 nm before cycling. [57] The stress due to the decomposition of LiPON electrolyte is calculated separately from the simulations of diffusion-induced-stress since the decomposition is summed to occur before the electrochemical reaction, such as during the film deposition process. [38] Therefore, the formation of the interphases is assumed as at time t=0 in this simulation.

2.4 Stress induced by the volume change from different sources

Assuming the volume change is isotropic, the chemical strain, $\boldsymbol{\varepsilon}_\mathrm{c}$, caused by the lithiation/de-lithiation of electrodes or the decomposition of the solid electrolyte is

$$\varepsilon_{c,ij} = (\sqrt[3]{1 + \Delta V} - 1)\delta_{ij} \quad \text{Eq. 10,}$$

with $\Delta \mathrm{V}$ being the volume change, $\Delta \mathrm{V_c}$ or $\Delta \mathrm{V_d}$, computed from Eq. 1 or Eq. 9, respectively. The induced stress is calculated based on static stress equilibrium and assuming linear isotropic elasticity:

$$\nabla \cdot \boldsymbol{\sigma} = 0 \qquad \text{Eq. 11,}$$

$$\boldsymbol{\sigma} = \boldsymbol{C} : \boldsymbol{\varepsilon}_{el} = \boldsymbol{C} : (\boldsymbol{\varepsilon} - \boldsymbol{\varepsilon}_c) \qquad \text{Eq. 12,}$$

$$\boldsymbol{\varepsilon} = \frac{1}{2}[\boldsymbol{\nabla u} + (\boldsymbol{\nabla u})^{\boldsymbol{T}}] \qquad \text{Eq. 13,}$$

where $\boldsymbol{\sigma}$ is the stress tensor, $\boldsymbol{\varepsilon}$ is the total strain tensor, $\boldsymbol{\varepsilon}_{el}$ is the elastic strain tensor, $\boldsymbol{u}$ is the displacement vector, and $\boldsymbol{C}$ is the fourth-order elasticity tensor that is a function of Young's modulus and Poisson's ratio.

The mechanical properties of different materials and the parameters used in this model are listed in Table A-1.

3 Results and discussion

3.1 Stress due to Li composition gradient during charging

To obtain the spatio-temporal lithium concentration evolution, the charging process of the 2.5D nanostructured ASSLB was simulated under three different current densities in accordance with corresponding experiments [28] (Figure 2). The resulting voltage evolution ($\varphi_{positive\_electrode} - \varphi_{negative\_electrode}$, from Eq. 6.) and terminal capacities of 0.038, 0.092, and 0.22 Ah/m^2 (evaluated at 4V) are in satisfactory agreement with the experimental results [28] as is the discharge curve (not shown), validating the parameters used in this model and giving credence to the predicted Li concentration profiles. Since the highest chemical stresses are expected to result from the largest Li concentration gradients, which in turn are occurring for faster charging rates, i.e. large current densities, only the highest simulated current density of 0.28 A/m^2 was considered in the following diffusion-induced-stress evaluations, this current density equals to 1.2 C-rate in this battery based on the projected electrode area according to the previous experimental study [28].

Figure 3 presents the respective Li concentration profile and flow directions early, intermediate, and late in the fastest charging process of Figure 2. Charging terminates due to the Li_yCoO_2 electrode reaching the y = 0.5 limit at 480 s. The final concentration change is confined to a relatively thin boundary layer close to the interfaces of the electrodes and the solid electrolyte. This corresponds to only a small fraction of the available Li being transported from the Li_yCoO_2 to the Li_xSi electrode, which is lithiated from x=1.68 to 2. Due to the selected termination criteria in the simulation, the egg carton geometry with a short distance between the top of the LCO electrode and the Si electrode results in low battery capacity since the limiting Li concentration is quickly reached at the top of the LCO electrode.

Figure 3 also shows the variation of Li-ion concentration in LiPON electrolyte is around $\pm 5\text{x}10^3$ mol/m^3, which is about 5% of the total Li-ion concentration ($1\text{x}10^5$ mol/m^3), confirming the negligible chemical strain in LiPON, as discussed in Section 2.2.

Based on the Li concentration profile at different times, the stress induced by the expansion/shrinking of electrodes was calculated for the two limiting boundary conditions and the results are shown in Figure 4. Consistent with the observed thin layers of de-lithiation in the LCO electrode, the thin layer of delithiated LCO electrode is under tensile stress, while the surrounding area is under compression. The area under compression (blue) in LCO increases with the charging time. Although there is no Li concentration induced strain in LiPON, the mechanical stress in LiPON electrolyte is mostly close to zero or slightly compressive. In comparison, the stress generated in the Si electrode is larger, since the volume change (or chemical strain) of Si electrode is more significant (~23% increase from 1.68 to 2 of Li ratio in Li_xSi) than that of LCO (-2% for Li decreasing from 1 to 0.5 in Li_yCoO_2). The thin lithiated Si layer is under compressive stress (blue), and the side regions (Si/LiPON) are under tensile stress (red). Since only a thin surface layer of Si is lithiated intensively, the rest of the Si is under slightly compressive stress due to a small amount of Li inserted. No substantial differences between the fixed (void-free battery) and free boundary conditions are observed except two small differences. The free boundary conditions allow a relaxation of the compressive (blue) stress induced in the volume above the top of the positive (LCO) electrode in the void-containing case. To accommodate the volume expansion of the lithiated Si, the LiPON near the Si developed higher tensile stress at the edges; this tensile stress is higher in free-side boundary conditions since the moving boundary facilitates tensile stress. At the end of charging, the largest tensile stress occurs in LiPON electrolyte instead of the Si electrode, which is due to the confined surfaces around Si, so the neighboring LiPON region is under more tensile stress.

3.2 Strain due to the Solid Electrolyte Decomposition

Table 1 lists the thermodynamically favored LiPON decomposition reactions and the corresponding molar volume change based on the DFT computed data collected in the Materials Project database, following the procedure listed in 2.3. Note that these are full reactions from the oxidation/reduction of the electrodes and electrolyte. These DFT predicted thermodynamically favored reactions may occur during the formation of the interface, during the cycling of the battery, or be limited by kinetics. Nevertheless, some reactions are indeed observed in experiments and they do provide the driving forces for interphase layer formation and suggest the electrochemical stability of the SE/electrode interface. The new phase formed due to the reactions are considered within a layer at the SE/electrode interface. The interphase layer can grow in thickness. But ideal solid electrolyte interphase will eventually stop growing as their electronic insulating nature will kinetically block the SE decomposition.

At the Li_2PO_2N/LixSi interface, as Si becomes lithiated, the Li voltage drops with increasing x in Li_xSi. So Li_2PO_2N decomposition reaction varies with respect to the lithium voltage with respect to metallic Li, as Si becomes LiSi, $Li_{12}Si_7$, Li_7Si_3, $Li_{13}Si_4$, and $Li_{21}Si_5$ [58, 59]. For all these Li_2PO_2N reduction reactions at the Li_xSi interface, as listed in Table 1, the volume shrinks. In this study, we focused on the “worst” cases within the range of Li ratio variation, as it is associated with the most significant volume changes of -27% at the Li_2PO_2N/LixSi interface, which occurs at the potential of $Li_{12}Si_7$. Based on the simulation of the charging process, the Li ratio varies from $Li_{1.68}Si$ to Li_2Si, suggesting this worst case will be reached experimentally.

At the Li_2PO_2N/Li_yCoO_2 interface, Li_2PO_2N is oxidized by Li_yCoO_2 and gas generation was predicted. In fact, bubbles (O_2 or N_2) formation has been found in the LiPON SE after applying a higher voltage in experiments [36]. In the present study, the volume of N_2 was excluded in the molar volume change, as gas may diffuse out. At the voltage above 3.63V, the most significant volume change is -8% at the $Li_2PO_2N/Li_{0.5}CoO_2$ interfaces, as listed in Table 1.

Therefore, on both the positive electrode side (Li_yCoO_2) and the negative electrode side (Li_xSi), the interphase layer formation entails a volume shrinkage. So, the corresponding chemical strain due to the decomposition of Li_2PO_2N at the negative and positive electrode side is -8.3% and -2%, respectively, based on Eq. 10.

3.3 Stress due to the Solid Electrolyte Decomposition

Figure 5 shows the first principal stress generated due to the formation of a 10 nm and 50 nm thick interphase layer, which was formed by the decomposition of the solid electrolyte at the electrode/SE interfaces. Table 2 collects the maximum first principal stress in different domains and under both boundary conditions.

From the results shown in Figure 5, the volume shrinkage due to the interphase formation causes tensile stress in the most part of the ASSLB. The magnitude of the stress and the region with high stress (higher than 3 GPa) increases with the thickness of the interphase layer. For an interphase layer of 10 nm, the stresses are minimal outside of the interphase layer. When the interphase layer thickness increases to 50 nm, most regions are under significantly higher tensile stresses. The LCO interphase generates stress of magnitude around ~3 GPa similarly under the two boundary conditions. The Si and LiPON experience higher stress levels with the fixed side than the free side conditions. The large stress level above 3 GPa corresponds to 3%, 1.5% and 3.8% of elastic strain in Si, Li_2CO_3, and LiPON, respectively. This stress level is beyond the elastic limit and can lead to fractures in these materials, especially in LiPON.

The voids seen in the 2.5D nanostructured ASSLB had an impact on stress development and affected the maximum stress in the electrolyte. The maximum stress generated by the same 50 nm interphase layer formation but under different boundary conditions, fixed and free void side, is compared in Table 2. A similar level of stress distribution and peak stress on the top region of the LCO electrode are observed for both cases. The continuous Si and LiPON top film in the 2.5D nanostructured ASSLB has a bridge region on top of the void. The center of the bridge is at the two sides of the Si and top LiPON phases in the model. The peak stress in Si and LiPON is developed in this region. Inside the Si, the maximum first principal stress does not change much with the boundary condition, while larger regions with tensile stress higher than 3GPa can be found under fixed side boundary conditions. The highest stress in the solid electrolyte drops significantly from 26.8 under the fixed side condition to 12.1 GPa under free side condition. These values will be sensitive to the details of the ASSLB structure and boundary conditions.

The simulated stress induced by the interphase layer formation reveals the importance of the thickness of interphase layers. The thickness of the interphase layer determines how large the region is affected by the decomposition: with 10 nm decomposition layer showing not much of an influence, while the regions with stresses higher than 3GPa is much larger for a 50 nm thick interphase layer. In this specific case (Si-LiPON-$LiCoO_2$), most of the stress occurred on the top of the battery because the volume change of the decomposition of LiPON electrolyte (-27%) is much more significant than that of LCO side (-8%). This decomposition-induced stress could be different when using different material combinations and applied potential and depends on the equilibrium interphases on both electrode/electrolyte interfaces.

4 Discussion

Other than the stress distribution, it is also informative to compare the maximum first principal tensile stresses in different domains and conditions, as shown in Figure 6. The decomposition-induced stress was considered to be generated at the beginning of the cycling, and the charging-induced stress increased with charging time. The comparison shows that the decomposition-induced stress would be more significant than the charging-induced stress if there are no voids in this battery, especially in the LiPON electrolyte. One interesting result with the charging-induced stress, it seems like irrespective of whether the side surfaces are fixed or not, the maximum stress all domains are very similar. These results show that the decomposition of electrolyte could cause more damage than the cycling of the batteries in terms of the mechanical failure in this specific battery geometry and material combinations. In either case, the LiPON electrolyte is the one that is most likely to have crack propagation since it is where the maximum first principal stress is generated. With some cracks, the battery can still function if the conductive pathways for Li ion and electrons are still available. However, the impedance becomes higher as more cracks/damages are generated, as shown in recent experiments by Lee et al. [2]. They also show the cracks are generated from the electrode/solid-electrolyte interface, consistent with our modeling results.

This mechanical failure depends on the material combinations in all-solid-state batteries and the architecture design. For systems that likely to have the decomposition of solid electrolytes, coatings can be applied to stabilize the electrode/solid-electrolyte interface and reduce solid electrolyte decomposition.[60-62] To release the mechanical constraints in ASSLB, softer materials such as polymer solid-electrolyte or polymer-based composite electrolyte can mitigate the stress generation.[63-65] In addition, the ASSLB architecture optimization, such as conformal architectures or internal voids intentionally, will be necessary to minimize the stress generation in order to mitigate mechanical failures.[66-68]

Conclusion

Although mechanical failures and cracks are potentially more detrimental in ASSLB compared to traditional liquid electrolyte based Li-ion batteries, the related studies are limited. To evaluate the induced-stress in ASSLB, we developed a 3D continuum model with Finite Element Analysis and incorporated two different sources of induced-stress in a 2.5D ASSLB: volume change from the decomposition of LiPON electrolyte and electrode expansion/contraction due to Li insertion/extraction. The decomposition of LiPON and the formation of 50 nm interphase layers caused -27% and -8% reduction in volume at the Si electrode and LCO electrode interfaces, respectively, and generated tensile stress higher than 3 GPa in most of the regions in the ASSLB. However, if voids exist on the sides in between the battery units, the maximum first principal stress in the solid electrolyte could be effectively reduced. On the other hand, the induced-stress from the expansion of the Si electrode and the contraction of the LCO electrode while charging is smaller, and only affected the surface layer of LCO, and inside LiPON near the Si. The maximum stress from charging is similar no matter the voids exist or not. These results suggest the chemical-stress from the decomposition of solid electrolytes could cause more damage to the ASSLB than the electrochemical cycling. Both will depend largely on the electrode/electrolyte materials used in ASSLB. Furthermore, this continuum model can be used for evaluating the induced stresses for different material combinations and different architecture of ASSLB to develop reliable, high energy density ASSLBs.

5 Acknowledgments

This work was supported by the funding from the Nanostructures for Electrical Energy Storage (NEES), an Energy Frontier Research Center funded by the U.S. Department of Energy, Office of Science, and Basic Energy Sciences under Award number DESC0001160. Sandia National Laboratories is a multi-mission laboratory managed and operated by National Technology and Engineering Solutions of Sandia, LLC., a wholly owned subsidiary of Honeywell International, Inc., for the US Department of Energy's National Nuclear Security Administration under contract DE-NA-0003525. The views expressed in the article do not necessarily represent the views of the US Department of Energy or the United States Government.

Tables

Table 1.Grand potential equilibrium phases of Li_2PO_2N

	voltage	Corresponding reaction	Volum change
Against Li_xSi	0–0.01	$21\ Li_2PO_2N + 8\ Li_{21}Si_5 \rightarrow 42\ Li_2O + 21\ Li_3N + 21\ Li_3P + 40\ Si$	-19%
	0.01–0.53	$52\ Li_2PO_2N + 24\ Li_{13}Si_4 \rightarrow 104\ Li_2O + 13\ Li_7PN_4 + 39\ Li_3P + 96Si$	-24%
		$28\ Li_2PO_2N + 24\ Li_7Si_3 \rightarrow 56\ Li_2O + 7\ Li_7PN_4 + 21\ Li_3P + 72\ Si$	-23%
		$4\ Li_2PO_2N + 2\ Li_{12}Si_7 \rightarrow 8\ Li_2O + Li_7PN_4 + 3\ Li_3P + 14\ Si$	**-27%**
		$4\ Li_2PO_2N + 24\ LiSi \rightarrow 8\ Li_2O + Li_7PN_4 + 3\ Li_3P + 24\ Si$	-29%
	0.53–0.65	$6\ Li_2PO_2N + 32\ LiSi_3 \rightarrow Li_{14}P_2(N_2O)_3 + 9\ Li_2O + 4\ Li_3P + 96\ Si$	-22%
Against Li_yCoO_2	2.64–3.04	$7\ Li_2PO_2N + 24\ Li_{0.75}CoO_2 \rightarrow 2\ Li_4P_2O_7 + P_3N_5 +$ ~~N_2~~ $+ 24\ LiCoO_2$	-2%
	> 3.63	**$3\ Li_2PO_2N + 12\ Li_{0.5}CoO_2 \rightarrow P_2O_5 + PNO +$ ~~N_2~~ $+ 12\ LiCoO_2$**	**-8%**

Table 2. The maximum first principal stress in different domains and boundary conditions

Maximum first principal stress (GPa)		Interphase layer thickness	
		50 nm	10 nm
Fixed side	Si electrode	14.7	12.6
	LCO electrode	3.64	1.8
	LiPON electrolyte	26.8	9.90
Free side	Si electrode	14.5	12.5
	LCO electrode	3.34	1.68
	LiPON electrolyte	12.1	9.89

Figures

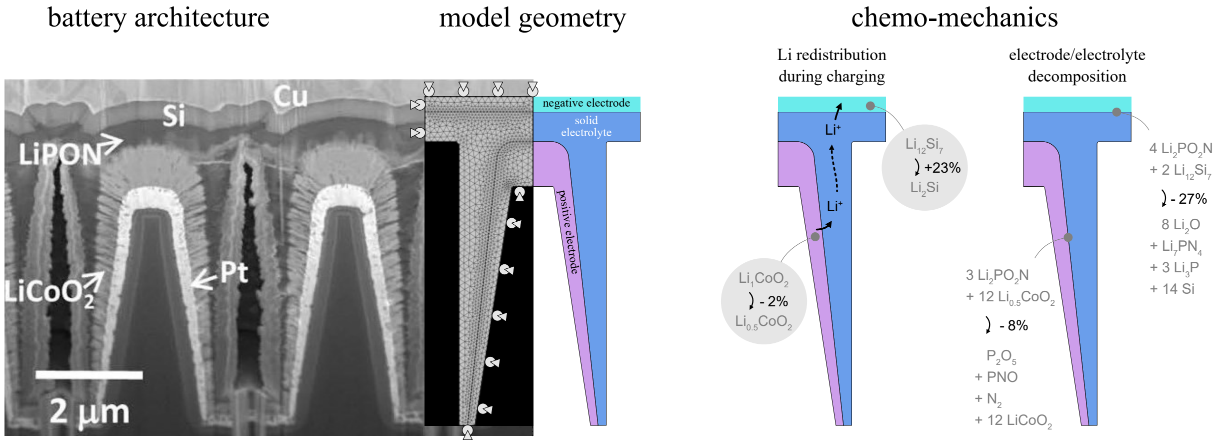

a) b) c) d)

Figure 1. (a) Focused ion beam cut cross-section of a hexagonally patterned 2.5D ASSLB; (b) its axially symmetric geometric simplification and computational mesh with boundary conditions for mechanical constraints, with "circle + triangle" symbols representing boundaries that are allowed to displace laterally but not normally to the boundaries; (c) reactions considered in the chemo-mechanical simulations that cause chemical strain due to Li transport and (d) due to interphase formation as a result of SE decomposition (d).

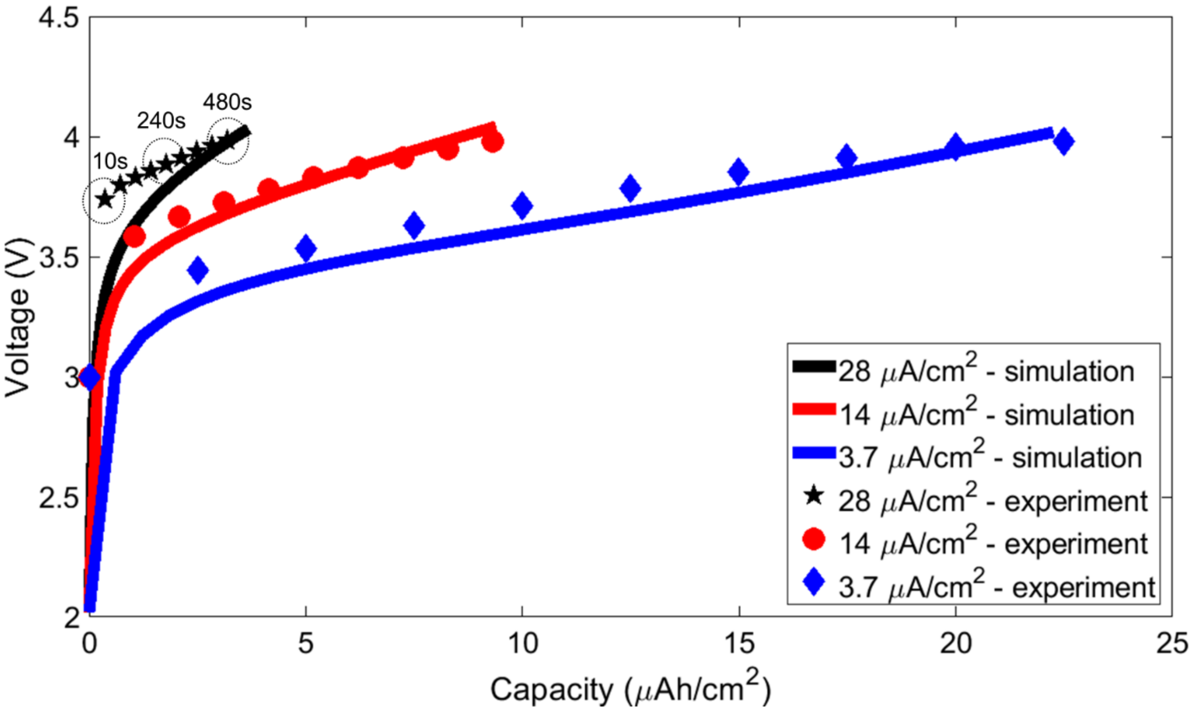

Figure 2. Simulated charging results for different charging rates (3.7, 14, 28 μA/cm^2, which equals to 0.16C, 0.6C, and 1.2C based on the projected electrode area according to the previous experimental study [28]) in comparison to experimental results.

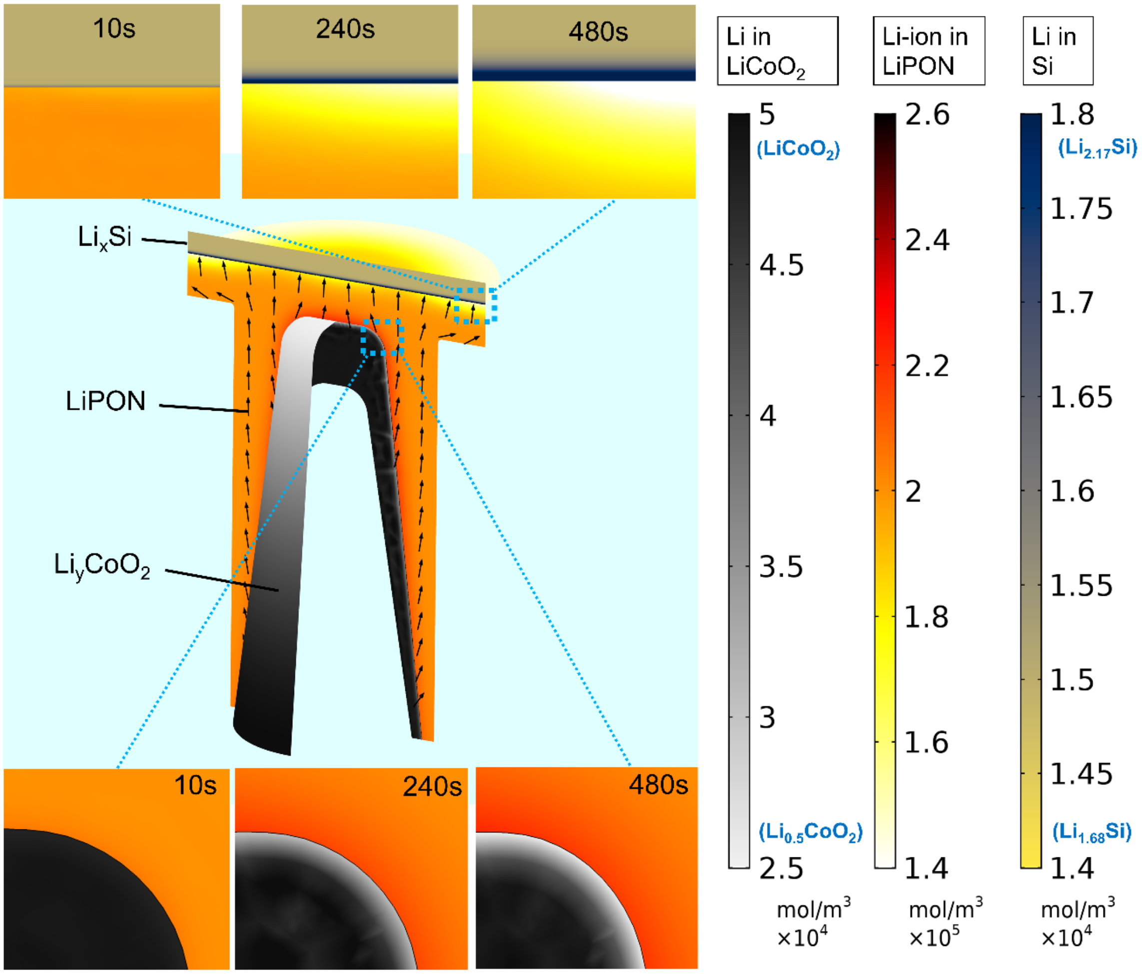

Figure 3. Li concentration profile at different times during charging at 0.28 A/m^2 (1.2C). The middle picture refers to the concentration profile at 240s, and the zoom-in sections show the change of Li concentration at different charging time. The arrows in the LiPON electrolyte represent the transport direction of Li-ions during charging.

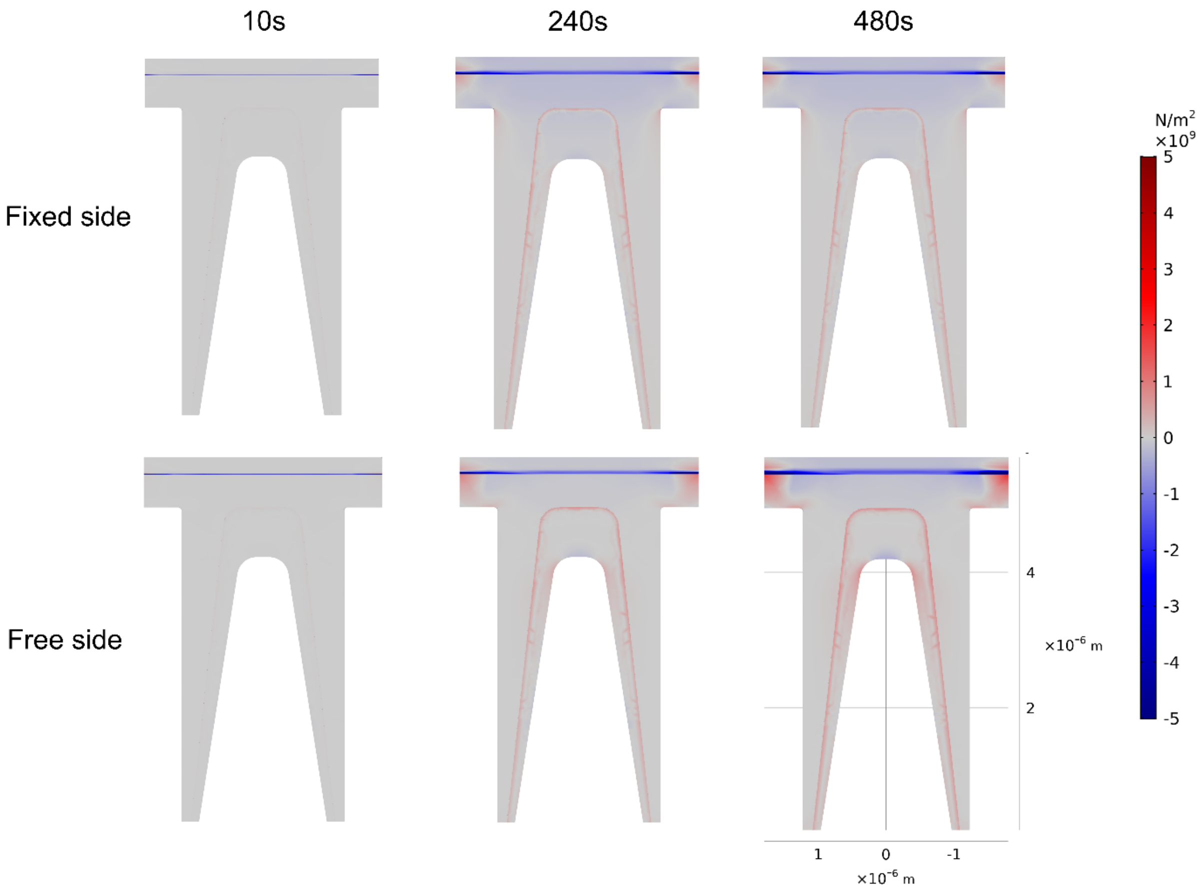

Figure 4. The first principal stress induced by the concentration change (see Figure 3) during the charging process. De-lithiation of LCO results in thin tensile (red) layer while lithiation of Si causes compressive (blue) stress for the two different situations, fixed side and free side (with voids) considered.

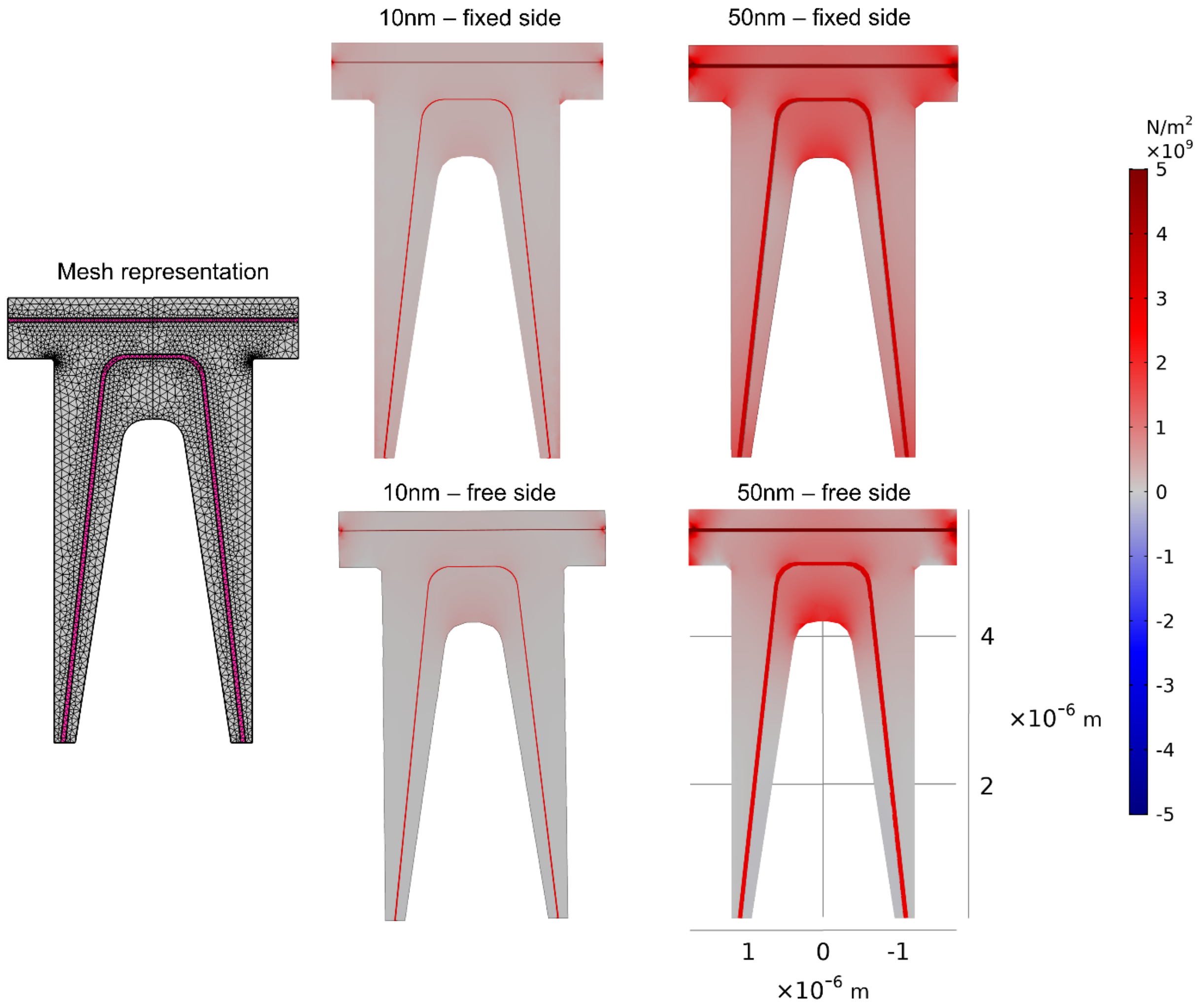

Figure 5. First principal stress induced from the decomposition of LiPON electrolyte for different boundary conditions and interphase thicknesses at t = 0s (red: tension). Mesh representation is for this simulation that includes two interphase layers (pink).

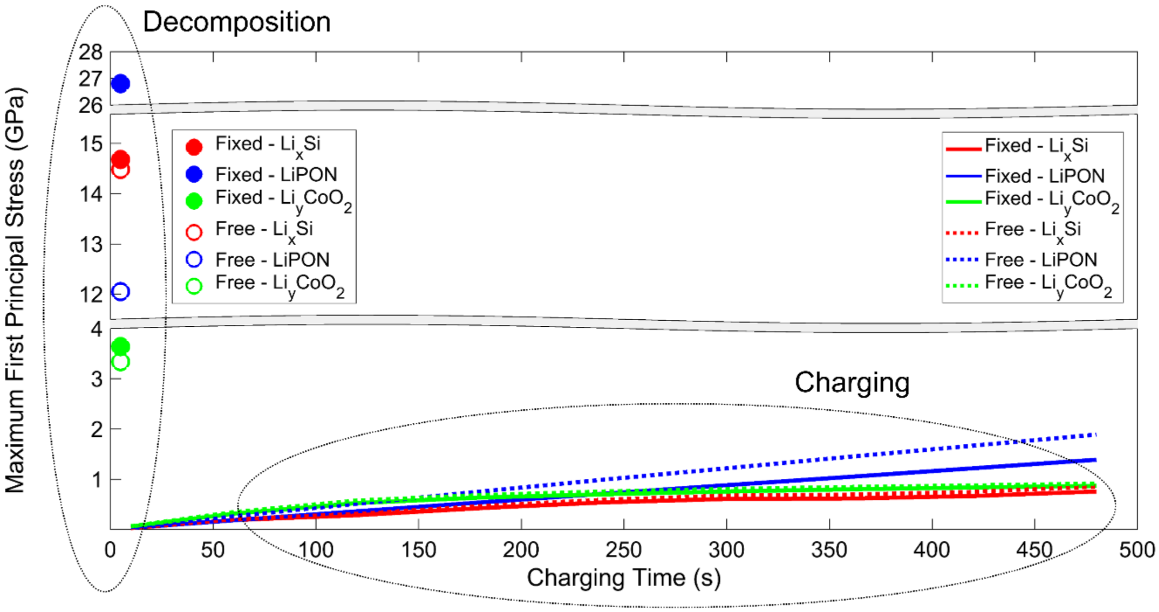

Figure 6. Comparison of maximum first principal stress from different sources and in different domains at different times during charging process at 28 μA/cm^2. The data of 50 nm interphase layer is used in this plot. Decomposition-induced stress occurs before charging the battery. The lines refer to the induced-stress during charging process, and the circle markers represent the stress from the decomposition of LiPON electrolyte.

Appendix A

Table A-1. Parameters used in this simulation. Most of the values were obtained either by fitting to experiments [28] or by DFT predictions [3]

Control variables	Description	Value
$C_{Li^+}^0$	Initial concentration of Li-ion in Li_2PO_2N electrolyte	2x10^4 [mol/m^3] [28]
$C_{Li\_negative}^0$	Initial concentration of Li in Li_xSi negative electrode	1.4x10^5 [mol/m^3] [28]
$C_{Li\_positive}^0$	Initial concentration of Li in Li_yCoO_2 positive electrode	4.9x10^4 [mol/m^3] [28]
$a_{v,Si}$	Volume change coefficient of Si electrode (within Si and $Li_{3.75}Si$)	8.45x10^{-4} [%/(mol·m^{-3})] [3]
$a_{v,LiCoO_2}$	Volume change coefficient of LCO electrode (within $Li_{0.5}CoO_2$ and $LiCoO_2$)	8x10^{-5} [%/(mol·m^{-3})] [3]
D_{Li_Si}	diffusion coefficient of Li in Li_xSi negative electrode	1x10^{-18} [m^2/s] [28]
$D_{Li\_LCO}^{normal}$	Normal diffusion coefficient of Li in Li_yCoO_2 positive electrode	2.5x10^{-18} [m^2/s] [28]
$D_{Li\_LCO}^{lateral}$	Lateral diffusion coefficient of Li in Li_yCoO_2 positive electrode	1x10^{-21} [m^2/s] [28]
D_{Li^+}	Diffusion coefficient of Li-ion in Li_2PO_2N electrolyte	5x10^{-17} [m^2/s] [28]
D_n	Diffusion coefficient of negative charge in Li_2PO_2N electrolyte	5x10^{-17} [m^2/s] [28]
$\alpha_{negative}$	Charge transfer coefficient at Li_xSi negative electrode	0.5 [28]
$\alpha_{positive}$	Charge transfer coefficient at Li_yCoO_2 positive electrode	0.5 [28]
$C_{Li\_negative\_max}$	Maximum concentration of Li-ion in Li_xSi negative electrode	3.11x10^5 [mol/m^3] [28]
$C_{Li\_negative\_min}$	Minimum concentration of Li-ion in Li_xSi negative electrode	0 [mol/m^3] [28]
$C_{Li\_positive\_max}$	Maximum concentration of Li-ion in Li_yCoO_2 positive electrode	5x10^4 [mol/m^3] [28]
$C_{Li\_positive\_min}$	Minimum concentration of Li-ion in Li_yCoO_2 positive electrode	2.5x10^4 [mol/m^3] [28]

$k_{negative}$	Kinetic constant at the negative electrode/electrolyte surface	1x10^{-2} [mol/(m^2·s)] [28]
$k_{positive}$	Kinetic constant at the positive electrode/electrolyte surface	1x10^{-4} [mol/(m^2·s)] [28]
Z_{Li^+}	Charge on Li-ion in Li_2PO_2N electrolyte	+1 [28]
Z_n	Charge on negative charge in Li_2PO_2N electrolyte	-1 [28]
E_{Si}	Young's modulus of Si electrode	96 [GPa] [3]
ν_{Si}	Poisson's ratio of Si electrode	0.29 [3]
ρ_{Si}	Density of Si electrode	2209 [kg/m^3] [69]
E_{LiCoO_2}	Young's modulus of $LiCoO_2$ electrode	191 [GPa] [70]
ν_{LiCoO_2}	Poisson's ratio of $LiCoO_2$ electrode	0.24 [70]
ρ_{LiCoO_2}	Density of $LiCoO_2$ electrode	4790 [kg/m^3] [70]
E_{LiPON}	Young's modulus of LiPON electrolyte	77 [GPa] [71]
ν_{LiPON}	Poisson's ratio of LiPON electrode	0.25 [71]
ρ_{LiPON}	Density of LiPON electrode	2300 [kg/m^3] [72]
A	Cross-section area of the Si electrode	1.02x10^{-11} [m^2] [28]

$$E_{negative}(a) = -4.76 \cdot a^6 + 9.34 \cdot a^5 - 1.8 \cdot a^4 - 7.13 \cdot a^3 + 5.8 \cdot a^2 - 1.94 \cdot a + 0.62$$

Eq. 14,

$$E_{positive}(b) = \frac{207.168 \cdot b^{10} - 467.807 \cdot b^8 + 354.911 \cdot b^6 - 198.242 \cdot b^4 + 322.003 \cdot b^2 - 219.027}{80.310 \cdot b^{10} - 182.567 \cdot b^8 + 113.081 \cdot b^6 - 3.43 \cdot b^4 + 35.463 \cdot b^2 - 44.337}$$

Eq. 15,

where a and b is the Li ratio in the negative electrode and positive electrode as $a = \frac{c_{Li\_negative}}{c_{Li\_negative\_max}}$ $(0 - 3.75)$ and $b = \frac{c_{Li\_positive}}{c_{Li\_positive\_max}}$ (0.5 – 1).

References

1. Sethuraman, V.A., V. Srinivasan, A.F. Bower, and P.R. Guduru, *In situ measurements of stress-potential coupling in lithiated silicon.* Journal of The Electrochemical Society, 2010. **157**(11): p. A1253-A1261.
2. Lee, S.W., M.T. McDowell, L.A. Berla, W.D. Nix, and Y. Cui, *Fracture of crystalline silicon nanopillars during electrochemical lithium insertion.* Proceedings of the National Academy of Sciences, 2012. **109**(11): p. 4080-4085.
3. Qi, Y., L.G. Hector, C. James, and K.J. Kim, *Lithium concentration dependent elastic properties of battery electrode materials from first principles calculations.* Journal of The Electrochemical Society, 2014. **161**(11): p. F3010-F3018.
4. Koerver, R., W. Zhang, L. de Biasi, S. Schweidler, A.O. Kondrakov, S. Kolling, T. Brezesinski, P. Hartmann, W.G. Zeier, and J. Janek, *Chemo-mechanical expansion of lithium electrode materials–on the route to mechanically optimized all-solid-state batteries.* Energy & Environmental Science, 2018. **11**(8): p. 2142-2158.
5. Behrou, R. and K. Maute, *Numerical modeling of damage evolution phenomenon in solid-state lithium-ion batteries.* Journal of The Electrochemical Society, 2017. **164**(12): p. A2573-A2589.
6. Deshpande, R., Y.-T. Cheng, and M.W. Verbrugge, *Modeling diffusion-induced stress in nanowire electrode structures.* Journal of Power Sources, 2010. **195**(15): p. 5081-5088.
7. Siegel, J.B., A.G. Stefanopoulou, P. Hagans, Y. Ding, and D. Gorsich, *Expansion of lithium ion pouch cell batteries: Observations from neutron imaging.* Journal of The Electrochemical Society, 2013. **160**(8): p. A1031-A1038.
8. Barai, P., K. Smith, C.-F. Chen, G.-H. Kim, and P.P. Mukherjee, *Reduced order modeling of mechanical degradation induced performance decay in lithium-ion battery porous electrodes.* Journal of The Electrochemical Society, 2015. **162**(9): p. A1751-A1771.
9. Yang, H., F. Fan, W. Liang, X. Guo, T. Zhu, and S. Zhang, *A chemo-mechanical model of lithiation in silicon.* Journal of the Mechanics and Physics of Solids, 2014. **70**: p. 349-361.
10. Miehe, C., H. Dal, L.M. Schänzel, and A. Raina, *A phase-field model for chemo-mechanical induced fracture in lithium-ion battery electrode particles.* International Journal for Numerical Methods in Engineering, 2016. **106**(9): p. 683-711.
11. Roberts, S.A., V.E. Brunini, K.N. Long, and A.M. Grillet, *A framework for three-dimensional mesoscale modeling of anisotropic swelling and mechanical deformation in lithium-ion electrodes.* Journal of The Electrochemical Society, 2014. **161**(11): p. F3052-F3059.
12. Huttin, M. and M. Kamlah, *Phase-field modeling of stress generation in electrode particles of lithium ion batteries.* Applied Physics Letters, 2012. **101**(13): p. 133902.
13. Li, J., K. Adewuyi, N. Lotfi, R.G. Landers, and J. Park, *A single particle model with chemical/mechanical degradation physics for lithium ion battery State of Health (SOH) estimation.* Applied energy, 2018. **212**: p. 1178-1190.
14. Thangadurai, V., S. Narayanan, and D. Pinzaru, *Garnet-type solid-state fast Li ion conductors for Li batteries: critical review.* Chemical Society Reviews, 2014. **43**(13): p. 4714-4727.
15. Agrawal, R. and G. Pandey, *Solid polymer electrolytes: materials designing and all-solid-state battery applications: an overview.* Journal of Physics D: Applied Physics, 2008. **41**(22): p. 223001.
16. Sun, C., J. Liu, Y. Gong, D.P. Wilkinson, and J. Zhang, *Recent advances in all-solid-state rechargeable lithium batteries.* Nano Energy, 2017. **33**: p. 363-386.
17. Song, J., Y. Wang, and C.C. Wan, *Review of gel-type polymer electrolytes for lithium-ion batteries.* Journal of power sources, 1999. **77**(2): p. 183-197.

18. Hassoun, J. and B. Scrosati, *Moving to a solid-state configuration: a valid approach to making lithium-sulfur batteries viable for practical applications.* Advanced Materials, 2010. **22**(45): p. 5198-5201.
19. Lewis, J.A., J. Tippens, F.J.Q. Cortes, and M.T. McDowell, *Chemo-Mechanical Challenges in Solid-State Batteries.* Trends in Chemistry, 2019.
20. Tippens, J., J. Miers, A. Afshar, J. Lewis, F.J.Q. Cortes, H. Qiao, T.S. Marchese, C.V. Di Leo, C. Saldana, and M.T. McDowell, *Visualizing Chemo-Mechanical Degradation of a Solid-State Battery Electrolyte.* ACS Energy Letters, 2019.
21. Lewis, J.A., F.J.Q. Cortes, M.G. Boebinger, J. Tippens, T.S. Marchese, N. Kondekar, X. Liu, M. Chi, and M.T. McDowell, *Interphase morphology between a solid-state electrolyte and lithium controls cell failure.* ACS Energy Letters, 2019. **4**(2): p. 591-599.
22. Chung, H. and B. Kang, *Mechanical and thermal failure induced by contact between a Li1. 5Al0. 5Ge1. 5 (PO4) 3 solid electrolyte and Li metal in an all solid-state Li cell.* Chemistry of Materials, 2017. **29**(20): p. 8611-8619.
23. Koerver, R., I. Aygün, T. Leichtweiß, C. Dietrich, W. Zhang, J.O. Binder, P. Hartmann, W.G. Zeier, and J.r. Janek, *Capacity fade in solid-state batteries: interphase formation and chemomechanical processes in nickel-rich layered oxide cathodes and lithium thiophosphate solid electrolytes.* Chemistry of Materials, 2017. **29**(13): p. 5574-5582.
24. Tian, H.-K. and Y. Qi, *Simulation of the Effect of Contact Area Loss in All-Solid-State Li-Ion Batteries.* Journal of The Electrochemical Society, 2017. **164**(11): p. E3512-E3521.
25. Li, W.J., M. Hirayama, K. Suzuki, and R. Kanno, *Fabrication and All Solid-State Battery Performance of TiS2/Li10GeP2S12 Composite Electrodes.* Materials Transactions, 2016. **57**(4): p. 549-552.
26. Ferrari, S., M. Loveridge, S.D. Beattie, M. Jahn, R.J. Dashwood, and R. Bhagat, *Latest advances in the manufacturing of 3D rechargeable lithium microbatteries.* Journal of Power Sources, 2015. **286**: p. 25-46.
27. Bates, J., N. Dudney, B. Neudecker, A. Ueda, and C. Evans, *Thin-film lithium and lithium-ion batteries.* Solid state ionics, 2000. **135**(1-4): p. 33-45.
28. Talin, A.A., D. Ruzmetov, A. Kolmakov, K. McKelvey, N. Ware, F. El Gabaly, B. Dunn, and H.S. White, *Fabrication, testing, and simulation of all-solid-state three-dimensional Li-ion batteries.* ACS applied materials & interfaces, 2016. **8**(47): p. 32385-32391.
29. Notten, P.H., F. Roozeboom, R.A. Niessen, and L. Baggetto, *3-D integrated all-solid-state rechargeable batteries.* Advanced Materials, 2007. **19**(24): p. 4564-4567.
30. Ruzmetov, D., V.P. Oleshko, P.M. Haney, H.J. Lezec, K. Karki, K.H. Baloch, A.K. Agrawal, A.V. Davydov, S. Krylyuk, and Y. Liu, *Electrolyte stability determines scaling limits for solid-state 3D Li ion batteries.* Nano letters, 2011. **12**(1): p. 505-511.
31. Arthur, T.S., D.J. Bates, N. Cirigliano, D.C. Johnson, P. Malati, J.M. Mosby, E. Perre, M.T. Rawls, A.L. Prieto, and B. Dunn, *Three-dimensional electrodes and battery architectures.* Mrs Bulletin, 2011. **36**(7): p. 523-531.
32. Bucci, G., T. Swamy, Y.-M. Chiang, and W.C. Carter, *Modeling of internal mechanical failure of all-solid-state batteries during electrochemical cycling, and implications for battery design.* Journal of Materials Chemistry A, 2017. **5**(36): p. 19422-19430.
33. Bucci, G., B. Talamini, A.R. Balakrishna, Y.-M. Chiang, and W.C. Carter, *Mechanical instability of electrode-electrolyte interfaces in solid-state batteries.* Physical Review Materials, 2018. **2**(10): p. 105407.
34. Kamaya, N., K. Homma, Y. Yamakawa, M. Hirayama, R. Kanno, M. Yonemura, T. Kamiyama, Y. Kato, S. Hama, and K. Kawamoto, *A lithium superionic conductor.* Nature materials, 2011. **10**(9): p. 682.

35. Liu, Z., W. Fu, E.A. Payzant, X. Yu, Z. Wu, N.J. Dudney, J. Kiggans, K. Hong, A.J. Rondinone, and C. Liang, *Anomalous high ionic conductivity of nanoporous β-Li3PS4.* Journal of the American Chemical Society, 2013. **135**(3): p. 975-978.
36. Yu, X., J. Bates, G. Jellison, and F. Hart, *A stable thin-film lithium electrolyte: lithium phosphorus oxynitride.* Journal of the electrochemical society, 1997. **144**(2): p. 524-532.
37. Zhu, Y., X. He, and Y. Mo, *Origin of outstanding stability in the lithium solid electrolyte materials: insights from thermodynamic analyses based on first-principles calculations.* ACS applied materials & interfaces, 2015. **7**(42): p. 23685-23693.
38. Zhu, Y.Z., X.F. He, and Y.F. Mo, *First principles study on electrochemical and chemical stability of solid electrolyte-electrode interfaces in all-solid-state Li-ion batteries.* Journal of Materials Chemistry A, 2016. **4**(9): p. 3253-3266.
39. Doyle, M., T.F. Fuller, and J. Newman, *Modeling of galvanostatic charge and discharge of the lithium/polymer/insertion cell.* Journal of the Electrochemical society, 1993. **140**(6): p. 1526-1533.
40. Fuller, T.F., M. Doyle, and J. Newman, *Relaxation phenomena in lithium-ion-insertion cells.* Journal of the Electrochemical Society, 1994. **141**(4): p. 982-990.
41. Fick, A., *V. On liquid diffusion.* The London, Edinburgh, and Dublin Philosophical Magazine and Journal of Science, 1855. **10**(63): p. 30-39.
42. Probstein, R.F., *Physicochemical hydrodynamics: an introduction*. 2005: John Wiley & Sons.
43. Danilov, D., R.A.H. Niessen, and P.H.L. Notten, *Modeling All-Solid-State Li-Ion Batteries.* Journal of the Electrochemical Society, 2011. **158**(3): p. A215-A222.
44. Bard, A.J., L.R. Faulkner, J. Leddy, and C.G. Zoski, *Electrochemical methods: fundamentals and applications*. Vol. 2. 1980: wiley New York.
45. Sethuraman, V.A., V. Srinivasan, and J. Newman, *Analysis of electrochemical lithiation and delithiation kinetics in silicon.* Journal of the Electrochemical Society, 2013. **160**(2): p. A394-A403.
46. Cheng, Y.-T. and M.W. Verbrugge, *Evolution of stress within a spherical insertion electrode particle under potentiostatic and galvanostatic operation.* Journal of Power Sources, 2009. **190**(2): p. 453-460.
47. Malavé, V., J. Berger, and P. Martin, *Concentration-dependent chemical expansion in lithium-ion battery cathode particles.* Journal of Applied Mechanics, 2014. **81**(9).
48. Zhao, K., M. Pharr, J.J. Vlassak, and Z. Suo, *Fracture of electrodes in lithium-ion batteries caused by fast charging.* Journal of Applied Physics, 2010. **108**(7): p. 073517.
49. Koyama, Y., T.E. Chin, U. Rhyner, R.K. Holman, S.R. Hall, and Y.M. Chiang, *Harnessing the actuation potential of solid-state intercalation compounds.* Advanced Functional Materials, 2006. **16**(4): p. 492-498.
50. Chakraborty, A., M. Dixit, D. Aurbach, and D.T. Major, *Predicting accurate cathode properties of layered oxide materials using the SCAN meta-GGA density functional.* npj Computational Materials, 2018. **4**(1): p. 1-9.
51. Kozen, A.C., A.J. Pearse, C.-F. Lin, M. Noked, and G.W. Rubloff, *Atomic layer deposition of the solid electrolyte LiPON.* Chemistry of Materials, 2015. **27**(15): p. 5324-5331.
52. George, S.M., *Atomic Layer Deposition: An Overview.* Chemical Reviews, 2010. **110**(1): p. 111-131.
53. Jain, A., S.P. Ong, G. Hautier, W. Chen, W.D. Richards, S. Dacek, S. Cholia, D. Gunter, D. Skinner, and G. Ceder, *Commentary: The Materials Project: A materials genome approach to accelerating materials innovation.* Apl Materials, 2013. **1**(1): p. 011002.
54. Ong, S.P., S. Cholia, A. Jain, M. Brafman, D. Gunter, G. Ceder, and K.A. Persson, *The Materials Application Programming Interface (API): A simple, flexible and efficient API for materials data based on REpresentational State Transfer (REST) principles.* Computational Materials Science, 2015. **97**: p. 209-215.

55. Peled, E. and S. Menkin, *SEI: past, present and future.* Journal of The Electrochemical Society, 2017. **164**(7): p. A1703-A1719.
56. Wang, A., S. Kadam, H. Li, S. Shi, and Y. Qi, *Review on modeling of the anode solid electrolyte interphase (SEI) for lithium-ion batteries.* npj Computational Materials, 2018. **4**(1): p. 15.
57. Santhanagopalan, D., D. Qian, T. McGilvray, Z. Wang, F. Wang, F. Camino, J. Graetz, N. Dudney, and Y.S. Meng, *Interface limited lithium transport in solid-state batteries.* The journal of physical chemistry letters, 2014. **5**(2): p. 298-303.
58. Lyalin, A., V.G. Kuznetsov, A. Nakayama, I.V. Abarenkov, I.I. Tupitsyn, I.E. Gabis, K. Uosaki, and T. Taketsugu, *Lithiation of Silicon Anode based on Soft X-ray Emission Spectroscopy: A Theoretical Study.* arXiv preprint arXiv:1801.01983, 2018.
59. Kim, H., C.-Y. Chou, J.G. Ekerdt, and G.S. Hwang, *Structure and properties of Li− Si alloys: a first-principles study.* The Journal of Physical Chemistry C, 2011. **115**(5): p. 2514-2521.
60. Ates, T., M. Keller, J. Kulisch, T. Adermann, and S. Passerini, *Development of an all-solid-state lithium battery by slurry-coating procedures using a sulfidic electrolyte.* Energy Storage Materials, 2019. **17**: p. 204-210.
61. Nakamura, T., K. Amezawa, J.r. Kulisch, W.G. Zeier, and J.r. Janek, *Guidelines for all-solid-state battery design and electrode buffer layers based on chemical potential profile calculation.* ACS applied materials & interfaces, 2019. **11**(22): p. 19968-19976.
62. Yao, X., N. Huang, F. Han, Q. Zhang, H. Wan, J.P. Mwizerwa, C. Wang, and X. Xu, *High-Performance All-Solid-State Lithium–Sulfur Batteries Enabled by Amorphous Sulfur-Coated Reduced Graphene Oxide Cathodes.* Advanced Energy Materials, 2017. **7**(17): p. 1602923.
63. Porcarelli, L., C. Gerbaldi, F. Bella, and J.R. Nair, *Super soft all-ethylene oxide polymer electrolyte for safe all-solid lithium batteries.* Scientific reports, 2016. **6**: p. 19892.
64. Zhang, J., J. Zhao, L. Yue, Q. Wang, J. Chai, Z. Liu, X. Zhou, H. Li, Y. Guo, and G. Cui, *Safety-reinforced poly (propylene carbonate)-based All-solid-state polymer electrolyte for ambient-temperature solid polymer lithium batteries.* Advanced Energy Materials, 2015. **5**(24): p. 1501082.
65. Zekoll, S., C. Marriner-Edwards, A.O. Hekselman, J. Kasemchainan, C. Kuss, D.E. Armstrong, D. Cai, R.J. Wallace, F.H. Richter, and J.H. Thijssen, *Hybrid electrolytes with 3D bicontinuous ordered ceramic and polymer microchannels for all-solid-state batteries.* Energy & Environmental Science, 2018. **11**(1): p. 185-201.
66. Pearse, A., T. Schmitt, E. Sahadeo, D.M. Stewart, A. Kozen, K. Gerasopoulos, A.A. Talin, S.B. Lee, G.W. Rubloff, and K.E. Gregorczyk, *Three-dimensional solid-state lithium-ion batteries fabricated by conformal vapor-phase chemistry.* ACS nano, 2018. **12**(5): p. 4286-4294.
67. Pearse, A.J., T.E. Schmitt, E.J. Fuller, F. El-Gabaly, C.-F. Lin, K. Gerasopoulos, A.C. Kozen, A.A. Talin, G. Rubloff, and K.E. Gregorczyk, *Nanoscale solid state batteries enabled by thermal atomic layer deposition of a lithium polyphosphazene solid state electrolyte.* Chemistry of Materials, 2017. **29**(8): p. 3740-3753.
68. Hur, J.I., L.C. Smith, and B. Dunn, *High areal energy density 3D lithium-ion microbatteries.* Joule, 2018. **2**(6): p. 1187-1201.
69. Custer, J., M.O. Thompson, D. Jacobson, J. Poate, S. Roorda, W. Sinke, and F. Spaepen, *Density of amorphous Si.* Applied physics letters, 1994. **64**(4): p. 437-439.
70. Cheng, E.J., N.J. Taylor, J. Wolfenstine, and J. Sakamoto, *Elastic properties of lithium cobalt oxide (LiCoO2).* Journal of Asian Ceramic Societies, 2017. **5**(2): p. 113-117.
71. Herbert, E.G., W.E. Tenhaeff, N.J. Dudney, and G. Pharr, *Mechanical characterization of LiPON films using nanoindentation.* Thin Solid Films, 2011. **520**(1): p. 413-418.
72. Lacivita, V., N. Artrith, and G. Ceder, *Structural and Compositional Factors That Control the Li-Ion Conductivity in LiPON Electrolytes.* Chemistry of Materials, 2018. **30**(20): p. 7077-7090.